Alzheimer's & Dementia: Translational Research & Clinical Interventions 3 (2017) 166-176

Alzheimer's & Dementia

Featured Article

Targeting butyrylcholinesterase for preclinical single photon emission computed tomography (SPECT) imaging of Alzheimer's disease

Drew R. DeBay[a,b], George A. Reid[a], Ian R. Pottie[c,d], Earl Martin[c], Chris V. Bowen[b,e], Sultan Darvesh[a,b,c,f,*]

[a]*Department of Medical Neuroscience, Dalhousie University, Halifax, Nova Scotia, Canada*
[b]*Biomedical Translational Imaging Centre, Halifax, Nova Scotia, Canada*
[c]*Department of Chemistry and Physics, Mount Saint Vincent University, Halifax, Nova Scotia, Canada*
[d]*Department of Chemistry, Saint Mary's University, Halifax, Nova Scotia, Canada*
[e]*Department of Radiology, Dalhousie University, Halifax, Nova Scotia, Canada*
[f]*Department of Medicine, Dalhousie University, Halifax, Nova Scotia, Canada*

Abstract

Introduction: Diagnosis of Alzheimer's disease (AD) *in vivo*, by molecular imaging of amyloid or tau, is constrained because similar changes can be found in brains of cognitively normal individuals. Butyrylcholinesterase (BChE), which becomes associated with these structures in AD, could elevate the accuracy of AD diagnosis by focusing on BChE pathology in the cerebral cortex, a region of scant BChE activity in healthy brain.

Methods: *N*-methylpiperidin-4-yl 4-[^{123}I]iodobenzoate, a BChE radiotracer, was injected intravenously into B6SJL-Tg(APPSwFlLon, PSEN1*M146 L*L286 V) 6799Vas/Mmjax (5XFAD) mice and their wild-type (WT) counterparts for comparative single photon emission computed tomography (SPECT) studies. SPECT, computed tomography (CT), and magnetic resonance imaging (MRI) enabled comparison of whole brain and regional retention of the BChE radiotracer in both mouse strains.

Results: Retention of the BChE radiotracer was consistently higher in the 5XFAD mouse than in WT, and differences were particularly evident in the cerebral cortex.

Discussion: Cerebral cortical BChE imaging with SPECT can distinguish 5XFAD mouse model from the WT counterpart.

Keywords: Alzheimer's disease; Butyrylcholinesterase; Acetylcholinesterase; Single-photon emission computed tomography; Molecular imaging; Neuroimaging; ^{123}Iodine; Alzheimer mouse model with 5 familial mutations

1. Introduction

Alzheimer's disease (AD) is a common cause of dementia [1]. Presently, AD diagnosis is definitively confirmed at autopsy by detecting cerebral pathology including β-amyloid (Aβ) plaques and tau neurofibrillary tangles (NFTs) [2]. To improve clinical diagnosis, positron emission tomography (PET) molecular imaging has been used to visualize Aβ and NFT in living brain [3–9]. These agents represent a leap forward in detecting the presence of Aβ and tau pathology [10]. However, the presence of Aβ in cognitively normal individuals (10% at 50 years to 44% at 90 years) and NFTs in non-AD tauopathies limits the predictive value of these methods for AD diagnosis [10–16]. Although cognitively normal individuals with PET amyloid positivity may represent preclinical stages of AD, conversion to AD has not yet been shown [17,18]. Therefore, the need is great for biomarkers to enhance existing armamentarium for AD diagnosis.

Neuronal loss, particularly cholinergic, contributes to cognitive and behavioral symptoms of AD [19–21]. With

*Corresponding author. Tel.: (902) 473-2490; Fax: (902) 473-7133.
E-mail address: sultan.darvesh@dal.ca

http://dx.doi.org/10.1016/j.trci.2017.01.005

this, there is a decrease in levels of acetylcholinesterase (AChE) and an increase in the levels of the related enzyme butyrylcholinesterase (BChE), that accumulate in plaques and tangles in the brain [22,23]. This accumulation of BChE in plaques and tangles enables differentiation of AD from old age [23]. The observation that there is scant BChE detected histochemically in the normal cerebral cortex, but accumulates there in association with AD pathology, suggests an opportunity to detect this pathology during life by imaging BChE [24].

Pioneering work in cholinesterase imaging provided PET probes targeting AChE [25–30] and BChE [26,31,32]. For example, *N*-[^{11}C] methylpiperidin-4-yl acetate ([^{11}C] MP4A) could monitor AChE activity *in vivo* in the AD brain [33]. Imaging BChE met less success using the butyrate ester of *N*-[^{11}C]methylpiperidinol, which entered the brain, but without increased radioligand uptake in regions that typically accumulate BChE-associated AD plaques [26,31,34]. Moreover, decreased uptake in AD brain compared to normal brain was observed, in contrast to histochemical and isolation studies of this enzyme [23,25,35–38].

A recent autoradiographic study [39], using a cholinesterase radioligand, phenyl 4-[^{123}I]iodophenylcarbamate, was able to distinguish AD amyloid plaques from those found in the cerebral cortex of cognitively normal brains. However, in further *in vivo* studies, this radiotracer did not provide satisfactory brain retention. Prospective substrate-type ^{123}I SPECT radioligands containing the *N*-methylpiperidinol moiety were designed to prolong ligand-enzyme latencies [39,40]. *Ex vivo* autoradiographic evidence was earlier reported for *N*-methylpiperidin-4yl 4-[^{123}I] iodobenzoate, which, injected intravenously into a rat, entered the brain and labeled areas known to exhibit BChE activity in histochemical studies [40]. In the present study, we extend this work by using dynamic SPECT images to evaluate BChE engagement and compare uptake, retention, and brain distribution of *N*-methylpiperidin-4-yl 4-[^{123}I]iodobenzoate radiotracer in the B6SJL-Tg(APPSwFlLon, PSEN1*M146 L*L286 V) 6799Vas/Mmjax (5XFAD) mouse model compared to that in its wild-type (WT) counterpart [41]. The 5XFAD model accumulates Aβ plaques that have BChE activity, as in human AD [42,43]. This animal model has significant BChE pathology over an aggressive course of amyloidosis [43]. The increased activity of this enzyme in the brain, compared to the WT counterpart, makes this model well suited for examining the potential of BChE imaging agents preclinically, as a proof of principle. Significantly, higher radiolabel retention in the 5XFAD brain, particularly in the cerebral cortex, would hold promise for such agents as imaging biomarkers for AD diagnosis.

2. Materials and methods

Formal approval to conduct these experiments was obtained from the Dalhousie University Radiation Safety Committee (overseen by the Canadian Nuclear Safety Commission).

2.1. Synthesis/biochemical materials

Na^{123}I in 0.1 N NaOH was obtained from MDS Nordion. Other chemicals and solvents were purchased from Sigma Aldrich (Canada). Isoflurane gas mixtures were diluted with oxygen. Ultraviolet (UV) analysis was on Ultrospec 2100 pro UV/Visible Spectrophotometer (Biochrom) with Swift II software (Amersham). High-performance liquid chromatography (HPLC) purifications were on an Agilent 1260 Infinity HPLC with ZORBAX Eclipse XDB-C18, 4.6 × 250 mm, 5 μm column (Agilent Technologies), and a RediFrac fraction collector (Amersham Biosciences).

2.2. Enzyme specificity

To determine murine BChE specificity for *N*-methylpiperidin-4-yl 4-iodobenzoate [40], repetitive scans for change in absorbance used mouse serum as enzyme source. Briefly, in a quartz cuvette, to a reaction mixture of 0.1 M phosphate buffer (2 mL, pH 7.4) containing 0.1% gelatin; 5XFAD serum (200 μL); and either (1) 50%$_{(aq)}$ acetonitrile (60 μL, no inhibitor), (2) 1 mM ethopropazine (60 μL, BChE inhibitor), or (3)1 mM BW 284C51 (60 μL, AChE inhibitor) in 50%$_{(aq)}$ acetonitrile, and mixed [44]. Reaction was initiated with 1 mM *N*-methylpiperidin-4-yl 4-iodobenzoate in 50%$_{(aq)}$ acetonitrile (30 μL). The UV absorbance of each mixture was scanned from 200 to 300 nm every 30 minutes for a total of 3.5 hours.

2.3. Synthesis and labeling of radiotracer

Synthesis of *N*-methylpiperidinol-4-yl 4-[^{123}I]iodobenzoate was performed with modification of the procedure described previously [40]. Briefly, in a plastic microtube (250 μL), Na^{123}I (~157 MBq) in 0.1 M NaOH$_{(aq)}$ (17 μL) was diluted with 0.1 M NaOH$_{(aq)}$ (10 μL), then acidified with 0.1 M HCl$_{(aq)}$ (32 μL), followed by addition of *N*-methylpiperidin-4-yl 4-(tributylstannyl)benzoate in acetonitrile (50 μL, 4.6 mM). The reaction was initiated by adding *N*-chlorosuccinimide in acetonitrile (50 μL, 3 mM). After vortexing (7.5 minutes) the mixture at room temperature, 0.1 M NaOH$_{(aq)}$ was added (13 μL). Precursor and nonradioactive iodobenzoate established HPLC retention times. Radiolabeled product was purified using HPLC with 80% methanol$_{(aq)}$ at 2 mL/minute as eluent. Fractions were collected every 30 seconds for 10 minutes. Collected fractions containing pure *N*-methylpiperidinol-4-yl 4-[^{123}I]iodobenzoate were combined and solvent evaporated at 40°C under a stream of argon. The radiochemical yield, on average, was 83%, based on HPLC radiograms and was consistent with radioscanned thin-layer chromatography (TLC) experiments that determined radiochemical purity to be >98%. Radiotracer was re-dissolved in 0.9% saline (0.4 mL) for animal administration.

2.4. Animals

Mice were cared for according to guidelines set by the Canadian Council on Animal Care; research was approved by

Dalhousie University Committee on Laboratory Animals. Pairs of female WT (C57BL/6J × SJL/J F1, stock number: 100012-JAX) and male transgenic hemizygous 5XFAD mice [B6SJL-Tg(APPSwFlLon, PSEN1*M146 L*L286 V) 6799Vas/Mmjax, stock number: 006554-JAX] were obtained from The Jackson Laboratory (Bar Harbor, ME, USA) and cared for as described previously [43]. Imaging was performed during light phase of the light–dark cycle. A total of 5 female mice (5XFAD $n = 3$, WT $n = 2$) and 7 male mice (5XFAD $n = 4$, WT $n = 3$) were imaged; average age was 11.1 ± 1.1 months. This age group was chosen to ensure robust deposition of pathology to increase the likelihood of detecting differences in BChE activity between WT and 5XFAD mice.

2.5. SPECT/CT imaging

Mice were weighed immediately before imaging, anesthetized with 3% isoflurane in an induction chamber, restrained in a Tailveiner Restrainer (Braintree Scientific) while under a continuous stream of 1.5% isoflurane. Mice were secured in prone position in a magnetic resonance (MR)-compatible animal bed. *N*-methylpiperidin-4-yl 4-[^{123}I]iodobenzoate (17.65–44.77 MBq in 0.9% saline (140–200 μL)) was administered through a lateral tail vein catheter line and subsequently flushed with saline. Mice were wrapped in a blanket on a heated bed, maintained under continuous stream of 1.5%–2% isoflurane and respiration rate monitored for the duration of scan (SA Instruments Inc., Stony Brook, NY, USA). The mouse head region was centered on a 14 mm axial field of view (FOV); dynamic SPECT frames (four projections per frame) were acquired in super list mode (SLM) over three 5 minute windows followed by four 10 minute windows with a SPARK (Cubresa Inc., MB, Canada) single-head standalone benchtop SPECT scanner integrated with a Triumph XO LabPET preclinical computed tomography (CT) scanner (TriFoil Imaging, CA, USA). After initial scanner setup and homing cycle of the SPECT gantry, frame 1 commenced 3.5 minutes after injection with subsequent frames acquired on average at 3.5, 9.75, 16.0, 22.5, 33.75, 45.0, and 56.75 minutes. Following SPECT scanning, a CT scan was acquired for anatomical reference and subsequently coregistered with anatomical magnetic resonance imaging (MRI) acquired in a separate scan (see Section 2.6). CT images were collected in fly mode with a 70-kVp x-ray beam energy (160 μA beam current), 512 projections, four summed frames/projection, with 2 × 2 binning and magnification of 2.26X, providing complete whole-brain coverage in a 56-mm FOV. CT scan duration was 8.5 minutes.

2.6. MRI

MRI scans were performed in a separate session before SPECT/CT imaging to facilitate regional analyses of radiotracer retention in the brain. MRI was carried out as described in a previous MRI protocol [45]. Images [$(142\ \mu m)^3$, full brain coverage] were acquired at 3.0 T over 61 minutes using a 3D balanced steady-state free precession, (b-SSFP) imaging sequence (T2/T1-weighting).

2.7. Image processing

Dynamic SPECT images were reconstructed over each of seven frames acquired (three 5 minute frames and four 10 minute frames) as follows: SPECT SLM data were converted to list mode data using built-in Cubresa SPARK preprocessing routine at 160 keV with a 20% energy window applied. List mode data were reconstructed using an iterative 3D maximum-likelihood expectation maximization algorithm (nine iterations) using HiSPECT software (SciVis Inc.). Resultant SPECT images yielded an effective in-plane resolution of 0.7 mm. Dark image and quantitative calibrations were performed weekly for the duration of the study and applied to each image acquired.

CT images were reconstructed with a 512 × 512 × 512 image matrix over a 56 mm FOV using built-in optimum noise reconstruction procedures with the Triumph XO CT acquisition software, yielding images with $(102\ \mu m)^3$ isotropic resolution. Fusion of SPECT and CT images was achieved using established coordinate transformations between the two modalities, whose common coordinate frames were applied in AMIDE imaging analysis software [46]. Images were assessed by visual inspection to ensure accurate fusion results. MRI images underwent 3D maximum intensity projection processing of four-phase cycle frequencies and resulting reconstructed images were zero-padded (interpolated to higher resolution grid to increase the effective resolution and image quality) in ImageJ (NIH, USA).

2.8. SPECT/CT/MRI coregistration and dynamic SPECT regional analysis

Intermodality registration performed between SPECT/CT/MRI and a MR-based 3D digital mouse atlas permitted parcellation of the brain for regional analyses as described previously [45,47]. A six-parameter rigid body registration was performed between mouse MR and a standard brain from which the digital atlas was derived using Automated Image Registration 5.3.0 [48]. Higher spatial transformations (warping) were applied to standard brain and corresponding warped MR atlas. MRI and warped MR atlas, along with SPECT/CT–fused images, were imported into AMIDE, where affine registration between modalities was carried out [46].

SPECT regions of interest (ROI) statistics were generated to determine *N*-methylpiperidin-4-yl 4-[^{123}I]iodobenzoate retention for six ROIs defined by the MR atlas: (1) whole brain, (2) cerebral cortex, (3) hippocampal formation, (4) amygdala, (5) thalamus, and (6) basal ganglia. Composite ROIs were derived using fslmaths scripts using threshold and subtraction commands carried out in FSL (Oxford, UK). Whole-brain ROIs contained all atlas brain structures excluding the cerebellum and brainstem. "Rest-of-brain" masks were also generated for each brain structure investigated, comprised of whole brain excluding

the ROI of interest. *N*-Methylpiperidin-4-yl 4-[^{123}I]iodobenzoate retention values in raw time activity curves are reported as the average (mean voxel value) percent injected dose per mL of brain tissue (%ID/mL). Retention indices were computed for each ROI, expressed as relative standardized uptake values (SUVRs) with each rest-of-brain internal reference tissue (represented as $SUVR_{ROI} = SUV_{ROI}/SUV_{(whole\ brain\ -\ ROI)}$). This metric was used to limit any possible intersubject or interscan variability.

2.9. BChE histochemistry

Brain tissue processing and BChE histochemistry were carried out as described previously to generate photomicrographs of BChE distributions in 5XFAD and WT mouse brains [42].

2.10. Statistical analysis

Unpaired t-tests (single tailed, assuming unequal variances) of group means (5XFAD vs WT) were carried out at each time-activity curve interval for both %ID/mL and SUVR metrics. Differences were concluded at a significance level of 5% ($P < .05$, *), 1% ($P < .01$, **), and trends were identified at ($P < .10$, †). All data are presented as group means ± standard error of the mean (SEM). All statistical tests were performed in Excel (Microsoft Office, version 15.13.1).

3. Results

3.1. Synthesis of N-methylpiperidin-4-yl 4-[^{123}I] iodobenzoate

The radiotracer was prepared and purified using modifications to an earlier procedure [40]. Here, acetonitrile replaced methanol as reaction solvent to prevent ester methanolysis. Reaction time was reduced (15 minutes to 7.5 minutes) by continuous vortexing once reactants were combined. Better separation and purification of product by HPLC was effected by making the reaction mixture slightly alkaline with 0.1-M $NaOH_{(aq)}$ instead of $NaHCO_{3(aq)}$. These modifications provided radiochemical yields >80%, radiochemical purity >98%, and calculated specific activity of approximately 4500 GBq/μmol.

3.2. Cholinesterase specificity for 1-methylpiperidin-4-yl 4-iodobenzoate

The nonradioactive iodobenzoate was examined using mouse serum containing both AChE and BChE. As indicated in repetitive scans (Fig. 1A), the ester underwent slow hydrolysis at pH 7.4 over 210 minutes. When mouse serum was first treated with BChE inhibitor, ethopropazine, under the same conditions, no hydrolysis occurred (Fig. 1B) [44]. In contrast, AChE inhibitor, BW 184C51, showed no effect

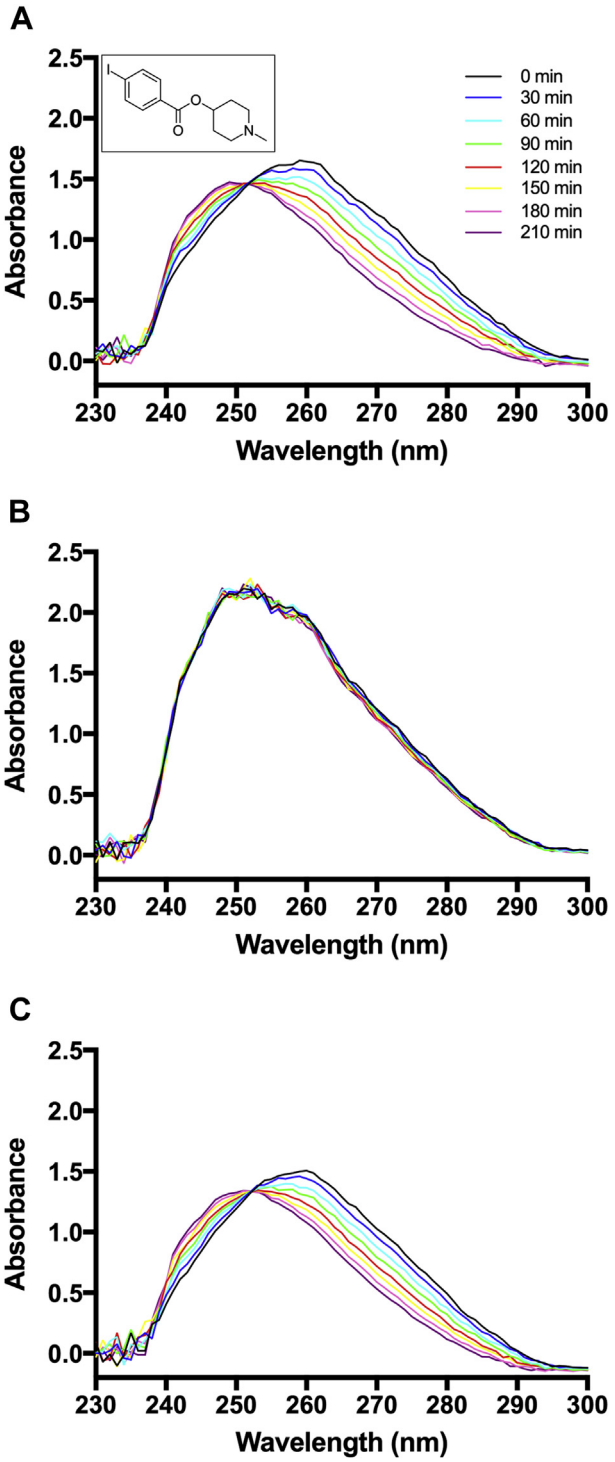

Fig. 1. 5XFAD mouse serum hydrolysis of *N*-methylpiperidin-4-yl 4-iodobenzoate demonstrated by repetitive UV scans at 30 minute intervals over 3.5 hours in 0.1 M phosphate buffer (pH 7.4). (A) Without inhibitor added (inlay shows probe chemical structure). (B) In the presence of BChE inhibitor ethopropazine. (C) In the presence of AChE inhibitor, BW 284C51. No effect on hydrolysis in the presence of BW 284C51. Abbreviations: AChE, acetylcholinesterase; BChE, butyrylcholinesterase; 5XFAD, B6SJL-Tg(APPSwFlLon, PSEN1*M146 L*L286 V) 6799Vas/Mmjax mouse strain; UV, ultraviolet.

on ester hydrolysis (Fig. 1C), indicating the iodobenzoate interacts with BChE over AChE [44].

3.3. Dynamic SPECT imaging

After injection of *N*-methylpiperidin-4-yl 4-[^{123}I]iodobenzoate, dynamic SPECT scans of mouse brain were

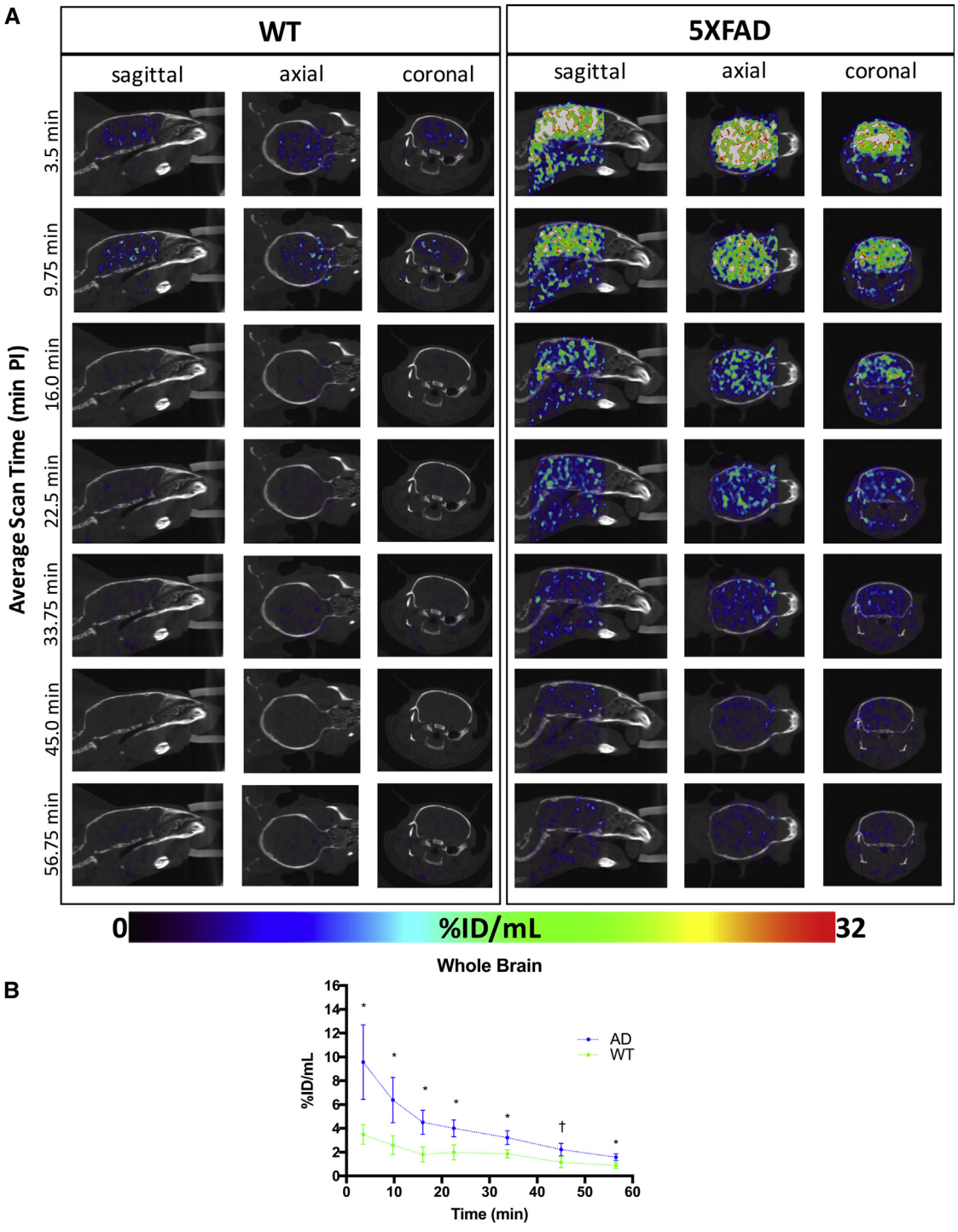

Fig. 2. (A) Representative WT (left) and 5XFAD (right) dynamic SPECT/CT brain images in sagittal, axial, and coronal planes. SPECT activity source maps indicate initial uptake and blood–brain barrier penetrance of radiotracer by 3.5 minute post-injection (PI) in both WT and 5XFAD brains, with greater radiotracer retention in the 5XFAD brain compared to WT. Image intensities expressed as percent injected dose per mL (%ID/mL) are set to a common color scale of 0%ID/mL–32%ID/mL. (B) Corresponding whole-brain radiotracer SPECT time-activity curves for 5XFAD (blue) and WT (green) mice (mean ± SEM). Significantly greater cerebral retention is evident in 5XFAD compared to WT. *Denotes statistically significant differences ($P < .05$); †Indicates a statistical trend ($P < .10$). Abbreviations: CT, computed tomography; SEM, standard error of the mean; WT, wild-type; 5XFAD, B6SJL-Tg(APPSwFlLon, PSEN1*M146 L*L286 V) 6799Vas/Mmjax mouse strain; SPECT, single photon emission computed tomography.

acquired over 60 minutes, divided into 5 and 10 minute frames. Dynamic SPECT frames generated 472,846 to 1,044,089 counts for 5 minute frames and 671,233 to 1,901,199 counts for 10 minute frames. These count levels provided sufficient signal-to-noise ratio and reconstructed image quality for assessment of brain uptake and retention of radiotracer. SPECT, CT, and MRI image registration provided robust and reproducible affine and nonlinear registration of these modalities with corresponding MR-based digital atlas [45]. From this, comparisons of brain retention of radiotracer could be assessed in 5XFAD and compared to WT mice.

3.4. Whole-brain retention of radioligand

Dynamic SPECT images (Fig. 2A) and corresponding time-activity curves (Fig. 2B) permitted semiquantitative comparison of radiotracer retention between 5XFAD and WT groups over the entire whole brain imaging session. Results described represent pooled male and female data because no sex differences were observed (separate analysis, not shown).

Both WT and 5XFAD strains showed rapid uptake of radiotracer into the brain (Fig. 2A and 2B), indicating it readily crossed the blood–brain barrier. Shown in the time-activity curves (Fig. 2B), by 3.5 minutes after ligand injection, radioactivity is clearly visible in both 5XFAD and WT mouse brains (Fig. 2A). Time-activity curves (Fig. 2B) indicate subsequent washout of radiotracer in 5XFAD and WT brains within 15–20 minutes after injection. In each time frame up to 60 minutes, there was greater (up to 2.3-fold) retention of label in 5XFAD brains relative to WT. Heterogeneous distribution of radiolabel throughout the whole brain (Fig. 2A) was evident. Distribution differences of radiolabel in WT and 5XFAD brains could reflect areas of high BChE-associated AD pathology. Radiotracer assessment of the regional distribution demonstrated specific patterns of retention that distinguish 5XFAD brains from WT controls.

3.5. Comparative histochemical- and SPECT-visualized regional butyrylcholinesterase activity

Histological analysis represents the "gold standard" for detection of BChE activity in brain tissue and indicates a heterogeneous distribution of the enzyme throughout the brain. For example, as observed in the normal human brain, WT mouse brain (Fig. 3, top) exhibits very little BChE histochemical staining in the cerebral cortex [23,38]. However, the cerebral cortex of 5XFAD shows marked BChE accumulation [42,43] (Fig. 3, bottom). Because both the cerebral cortex and subcortical regions, such as the hippocampal formation and thalamus, develop BChE-associated AD pathology, it may be assumed that a region such as the cerebral cortex, that normally has little BChE activity, may provide the greatest contrast for detecting BChE-associated AD pathology (Fig. 3) than would subcortical regions that express BChE in the absence of AD pathology. This notion is supported by semiquantitative analyses of SPECT radiolabel retention (Fig. 4). To compare potential differences in radiotracer retention between 5XFAD and WT brains, several different regional metrics were tested to generate time-activity curves. ROIs examined included the cerebral cortex, basal ganglia, hippocampal formation, amygdala, and thalamus (Figs. 3 and 4).

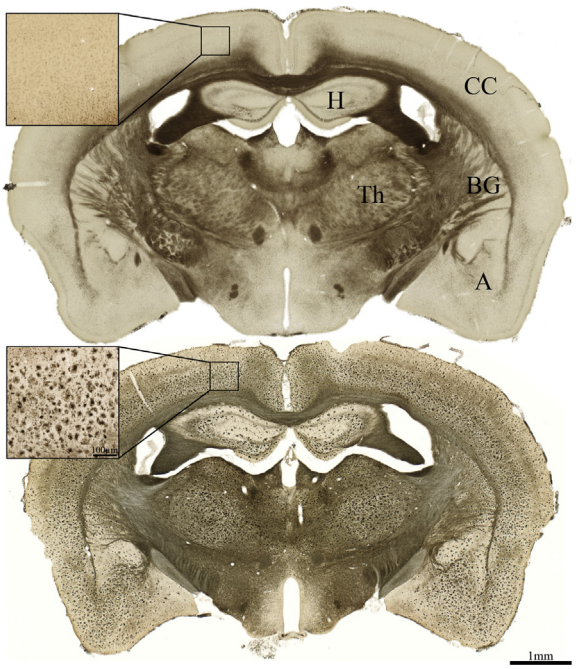

Fig. 3. Photomicrographs showing representative BChE histochemical staining at midcoronal level in WT (top) and 5XFAD (bottom) brains. Note little BChE staining in cerebral cortex of WT mice and marked elevation of BChE in cerebral cortex of 5XFAD mice. Significant accumulation of BChE in subcortical regions is also apparent, beyond that observed in the WT brain. Scale bar = 1 mm and 100 μm (inlay). Abbreviations: A, amygdala; BChE, butyrylcholinesterase; BG, basal ganglia; CC, cerebral cortex; H, hippocampal formation; Th, thalamus; WT, wild-type; 5XFAD, B6SJL-Tg(APPSwFlLon, PSEN1*M146 L*L286 V) 6799Vas/Mmjax mouse strain.

3.6. Cortical and subcortical retention comparisons

Time-activity curves for regional comparisons (Fig. 5) of 5XFAD and WT images (expressed as %ID/mL) showed similar trends in each ROI to observe for whole-brain evaluation (Fig. 2B). This was true for the cerebral cortex (Fig. 5A) as well as some subcortical structures (Fig. 5B–5E). It is evident that it depends on the ROI examined as to whether significant differences in retention of radiotracer could identify AD pathology through BChE association. For example, comparing robust retention in the cerebral cortex of 5XFAD relative to WT (Fig. 5A) with that in the amygdala (Fig. 5E), where there is no significant difference detected for the retention in the two strains. A summary graph of

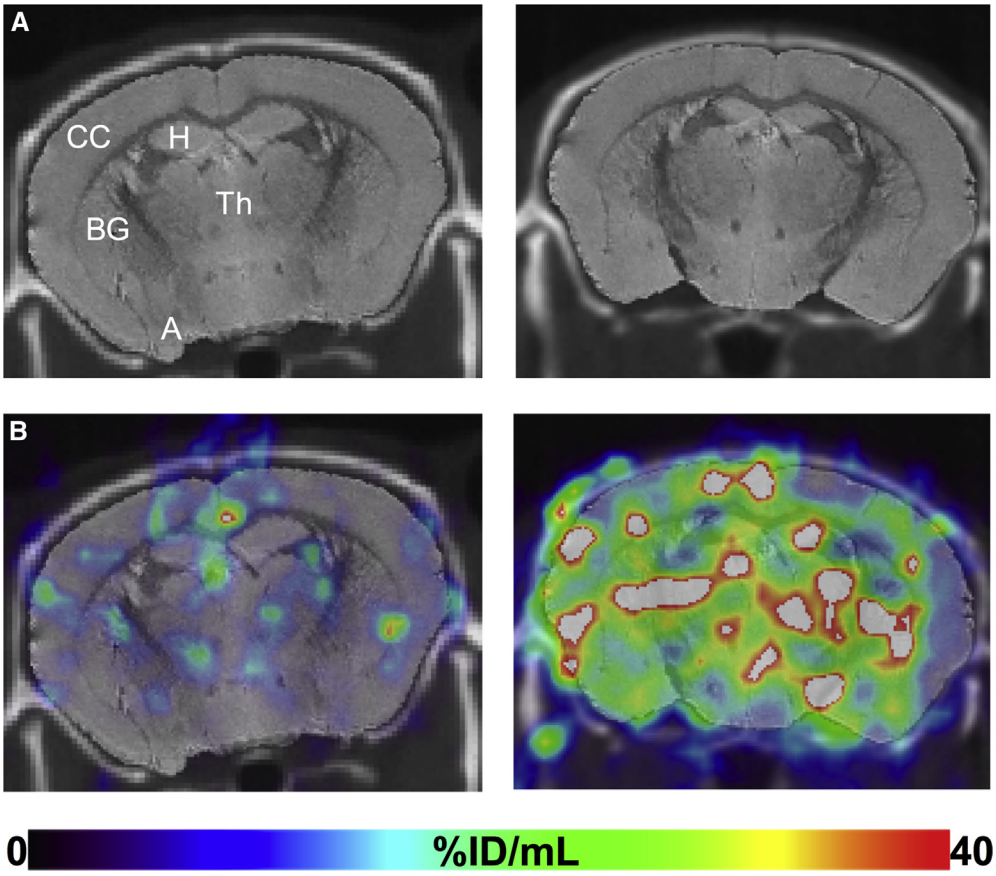

Fig. 4. Comparison of BChE activity at midcoronal level (as in Fig. 3) in specific brain regions of WT (left) and 5XFAD (right) mice detected with radiotracer SPECT analysis. (A) CT with coregistered MR. (B) SPECT images acquired at 4-minute post-injection with coregistered CT/MR and ROIs. Marked retention in the 5XFAD cerebral cortex is evident in the 5XFAD brain compared to WT with less difference in retention evident in amygdala, hippocampus, basal ganglia, and thalamus. Image intensities expressed as %ID/mL and set to a common scale of 0%ID/mL–40%ID/mL. Abbreviations: A, amygdala; BChE, butyrylcholinesterase; BG, basal ganglia; CC, cerebral cortex; CT, computed tomography; H, hippocampal formation; MR, magnetic resonance; ROIs, regions of interest; SPECT, single photon emission computed tomography; Th, thalamus; WT, wild-type; 5XFAD, B6SJL-Tg(APPSwFlLon, PSEN1*M146 L*L286 V) 6799Vas/Mmjax mouse strain.

fold difference in radiotracer retention between 5XFAD and WT time-activity curves is presented for the cerebral cortex and subcortical areas in Fig. 5F. All ROIs show the same trend of greater radiotracer retention in 5XFAD brain relative to WT save the amygdala. However, the greatest difference in radiotracer retention over time (~3-fold) is seen for the cerebral cortex. Because increased BChE accumulation in cerebral cortex is a prominent feature of AD progression, it is of value to assess the relative proportion of radiotracer in the brain that can be attributed to the cortex [22,23,38]. The cortical retention index, a relative SUV ($SUVR_{c.cortex/(whole\ brain\text{-}c.cortex)}$) metric that expresses tracer retention in the cortex normalized to radiotracer uptake in the rest of the brain, serves as a means to assess cortical retention while limiting interscan and intersubject variability between scans. With this metric, the cortical retention index was found to be significantly greater (18%–31%) in 5XFAD brain than in WT controls (Fig. 6A), which was sustained over the 60 minutes of study. This is indicated by the ratio of label retention in 5XFAD cerebral cortex over that of WT controls being consistently on the order of 1.2 to 1.3 over each time point examined (Fig. 6B).

4. Discussion

A number of approaches have been undertaken to develop biomarkers for definitive diagnosis of AD, including PET brain imaging of amyloid and tau. Several amyloid imaging agents have been approved as ancillary agents to test for AD and tau imaging agents are being developed [6–9]. However, because amyloid plaques and tau neurofibrillary tangles can also be found in cognitively normal individuals, development of additional biomarker targets seems imperative to improve the diagnosis of AD during life [10,11]. Changes in components of the cholinergic system, such as the appearance of BChE associated with AD pathology in the cerebral cortex, provide an opportunity to image this pathology without registering similar anomalies that may also be present in the brains of many cognitively normal individuals. Thus, BChE may represent a viable diagnostic imaging target which must be carefully considered. In other dementias, such as dementia with Lewy bodies and vascular dementia, there are no reported increases in levels of BChE [49,50]. However, for tauopathies, BChE radiotracers will need to be evaluated in appropriate mouse models to determine their specificity.

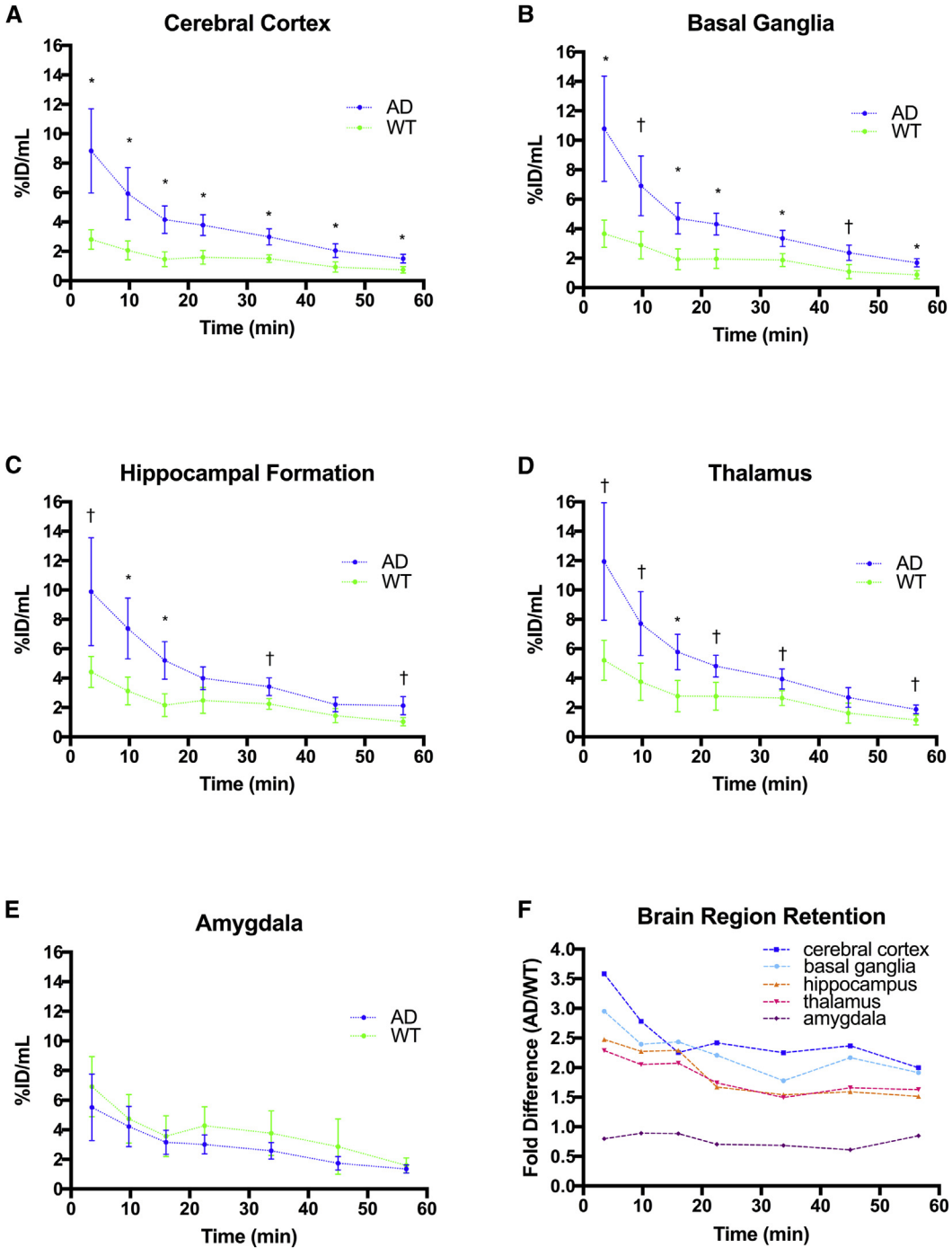

Fig. 5. Corresponding *N*-methylpiperidin-4-yl 4-[^{123}I]iodobenzoate time-activity curves for 5XFAD (blue) and WT (green) mice. Mean ± SEM. *Denotes statistically significant differences ($P < .05$), †Indicates a statistical trend ($P < .10$). (A) Sustained retention in the cerebral cortex over each dynamic frame was observed in 5XFAD compared to WT up to 60 minutes. (B) A similar trend of sustained retention was observed in basal ganglia up to 60 minutes. (C) Early retention in hippocampus was greater in the 5XFAD brain up to 30 minutes. (D) A similar trend of early retention was seen in the thalamus up to 30 minutes. (E) No differences were observed in amygdala retention between 5XFAD and WT over the entire time course. (F) Ratio of 5XFAD to WT time-activity curve means indicating the fold difference (increase) in radiotracer retention in the cerebral cortex (blue), basal ganglia (light blue), hippocampus (orange), thalamus (pink), and amygdala (purple) relative to WT controls. Cerebral cortex retention was approximately 3.5 fold greater at 4-minute post-injection and was maintained at approximately 2.5 fold up to 60-minute postinjection. Abbreviations: AD, Alzheimer's disease; SEM, standard error of the mean; WT, wild-type; 5XFAD, B6SJL-Tg(APPSwFlLon, PSEN1*M146 L*L286 V) 6799Vas/Mmjax (5XFAD).

The radiotracer *N*-methylpiperidin-4-yl 4-[^{123}I]iodobenzoate selectively engages with BChE and undergoes slow hydrolysis (Fig. 1). This radiotracer crosses the blood–brain barrier, and there is greater retention in brains of the 5XFAD mouse model than WT counterparts (Fig. 2). Dynamic SPECT imaging analysis measuring differential retention

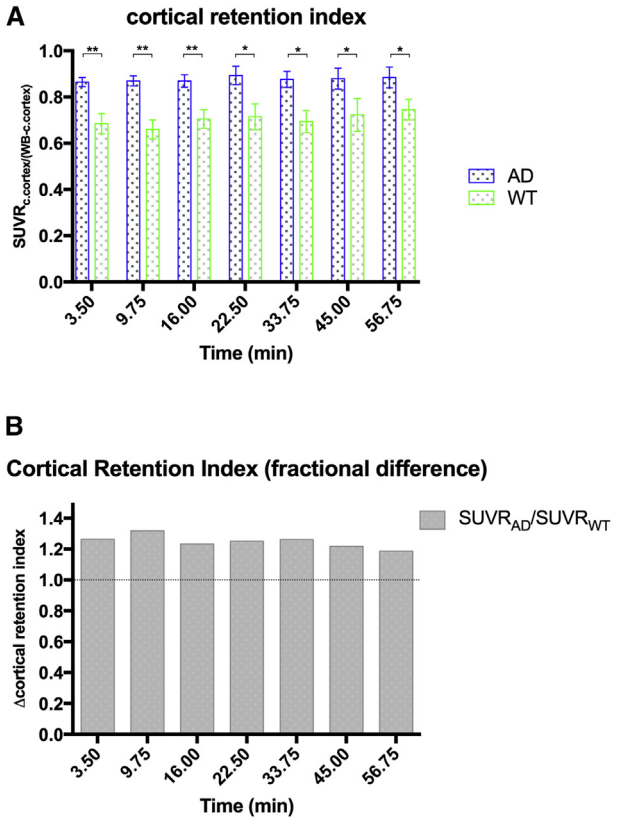

Fig. 6. A) *N*-methylpiperidin-4-yl 4-[^{123}I]iodobenzoate retention indices for 5XFAD (blue) and WT (green) mice. Mean ± SEM. (A) Cortical retention index ($SUVR_{c.cortex/(whole\ brain-c.cortex)}$: cortical retention normalized to rest-of-brain) was 18%–31% greater in 5XFAD brains versus WT over the 60-minute imaging window. *,**Denote statistically significant differences ($P < .05$, $P < .01$, respectively). (B) Fractional difference in cortical retention index between 5XFAD and WT indicating between 1.18–1.31X greater retention in the cerebral cortex of 5XFAD mice compared to WT. Abbreviations: AD, Alzheimer's disease; SEM, standard error of the mean; SUVR, relative standardized uptake value; WT, wild-type; 5XFAD, B6SJL-Tg(APPSwFlLon, PSEN1*M146 L*L286 V) 6799Vas/Mmjax mouse strain.

of radioactivity in the cerebral cortex and various subcortical regions (Fig. 4) revealed known histochemical BChE activity (Fig. 3). Time-activity curves derived from dynamic SPECT analysis consistently indicate elevated retention of radioactivity in brains of 5XFAD mice compared to WT counterparts (Figs. 2 and 5), that is particularly evident in the cerebral cortex (Figs. 5 and 6).

In previous attempts, *N*-methylpiperidinyl acetate and propionate could image AChE in the human brain, whereas *N*-methylpiperidinyl butyrate, a specific substrate for BChE, entered the brain and accumulated in certain regions [34], but it was unable to distinguish AD from normal brain [24,26–28,34]. It is not clear why *N*-methylpiperidinyl butyrate could not recapitulate what is known from postmortem brain histochemistry. There are several possibilities that include nonspecific or off-target binding of the tracer or that the radioactive atom (^{11}C) is located on the side of the ester molecule that is the first leaving group during the BChE-catalyzed hydrolysis. This could cause the radioactive atom being rapidly dispersed away from the target. To test this possibility, a radiotracer with a larger acyl group bearing the radioactive atom was used. The placement of the radioactive atom (^{123}I) on the acyl portion of the ester ensures a longer lived enzyme-acyl intermediate than the earlier ligands. Altering the placement of the radioactive atom appeared to improve the imaging outcomes in this study. More importantly, these findings are in keeping with earlier observations in human AD that BChE associates with AD pathology [23,35–37]. Evidence that BChE radiotracers can distinguish between AD pathology and that in cognitively normal brains with pathology bodes well for increased diagnostic performance with the development of selective BChE targeted imaging agents for comparative studies focused on the cerebral cortex [39].

4.1. Conclusions

These preliminary findings provide *in vivo* evidence of *N*-methylpiperidin-4-yl 4-[^{123}I]iodobenzoate crossing the blood–brain barrier and are suggestive of target engagement of this radioligand with BChE-associated pathology in the cerebral cortex of the 5XFAD brain. The present study demonstrates that BChE-specific radiotracers can be developed as AD diagnostic agents. This work opens avenues for further investigations to determine the temporal association of BChE accumulation in pathology using SPECT BChE radiotracers in this and other preclinical models and, ultimately, in human AD.

Acknowledgments

The authors would like to thank Christa Davis, Dr. Erin Mazerolle, and Selena Maxwell for their technical support and Dr. Steven Burrell for imaging discussions. This research was supported by the Canadian Institutes of Health Research (MOP-82798, RNS-117795, MOP-119343), Capital Health Research Fund, Nova Scotia Health Research Foundation (Scotia Scholar™, MED-MAT-2011-7512), Faculty and Department of Medicine of Dalhousie University, Natural Sciences and Engineering Research Council of Canada, Killam Trusts, Innovacorp, Mount Saint Vincent University Committee on Research and Publication (MSVU#120450), Dalhousie Medical Research Foundation Gunn Family Research Prize, DeWolfe Graduate Studentship, Mrs. Sadie MacLeod through the Dalhousie Medical Research Foundation Adopt-a-Researcher program and the Dalhousie Medical Research Foundation Irene MacDonald Sobey Endowed Chair in Curative Approaches to Alzheimer's Disease.
Sultan Darvesh is a scientific cofounder and stockholder in Treventis Corporation, a biotech company focused on development of diagnostic and therapeutic agents for Alzheimer's disease. Sultan Darvesh, Ian R. Pottie, and Earl Martin are listed as inventors on patents related to this work, and these patents are assigned to Treventis Corporation. The other authors have no financial disclosures or conflicts with this submission.

RESEARCH IN CONTEXT

1. Systematic review: A significant amount of effort in recent Alzheimer's disease (AD) research has been in the quest to identify noninvasive biomarkers (e.g., imaging) to assist in the early diagnosis of AD during life. The authors have reviewed the current state of AD neuroimaging research as well as the body of cholinesterase imaging research that has been investigated to date. These relevant citations are provided in this article.
2. Interpretation: We have identified a butyrylcholinesterase-specific radiotracer that crosses the blood–brain barrier, recapitulates the known histochemical distribution of butyrylcholinesterase-associated Alzheimer pathology and has potential to augment current clinical and brain imaging diagnostics toward an early and definitive diagnosis of AD.
3. Future directions: These preliminary results warrant further study to refine our understanding of the detailed imaging characteristics of this and similar classes of butyrylcholinesterase radiotracers.

References

[1] Scheltens P, Blennow K, Breteler MM, de Strooper B, Frisoni GB, Salloway S, et al. Alzheimer's disease. Lancet 2016;388:505–17.

[2] Hyman BT, Trojanowski JQ. Consensus recommendations for the postmortem diagnosis of Alzheimer disease from the National Institute on Aging and the Reagan Institute Working Group on diagnostic criteria for the neuropathological assessment of Alzheimer disease. J Neuropathol Exp Neurol 1997;56:1095–7.

[3] McKhann GM, Knopman DS, Chertkow H, Hyman BT, Jack CR Jr, Kawas CH, et al. The diagnosis of dementia due to Alzheimer's disease: recommendations from the National Institute on Aging-Alzheimer's Association workgroups on diagnostic guidelines for Alzheimer's disease. Alzheimers Dement 2011;7:263–9.

[4] Bloudek LM, Spackman DE, Blankenburg M, Sullivan SD. Review and meta-analysis of biomarkers and diagnostic imaging in Alzheimer's disease. J Alzheimers Dis 2011;26:627–45.

[5] Klunk WE, Engler H, Nordberg A, Wang Y, Blomqvist G, Holt DP, et al. Imaging brain amyloid in Alzheimer's disease with Pittsburgh Compound-B. Ann Neurol 2004;55:306–19.

[6] Zhang W, Oya S, Kung MP, Hou C, Maier DL, Kung HF. F-18 Polyethyleneglycol stilbenes as PET imaging agents targeting Abeta aggregates in the brain. Nucl Med Biol 2005;32:799–809.

[7] Zhang W, Oya S, Kung MP, Hou C, Maier DL, Kung HF. F-18 stilbenes as PET imaging agents for detecting beta-amyloid plaques in the brain. J Med Chem 2005;48:5980–8.

[8] Serdons K, Terwinghe C, Vermaelen P, Van Laere K, Kung H, Mortelmans L, et al. Synthesis and evaluation of 18F-labeled 2-phenylbenzothiazoles as positron emission tomography imaging agents for amyloid plaques in Alzheimer's disease. J Med Chem 2009;52:1428–37.

[9] Villemagne VL, Fodero-Tavoletti MT, Masters CL, Rowe CC. Tau imaging: early progress and future directions. Lancet Neurol 2015;14:114–24.

[10] Johnson KA, Minoshima S, Bohnen NI, Donohoe KJ, Foster NL, Herscovitch P, et al. Appropriate use criteria for amyloid PET: a report of the Amyloid Imaging Task Force, the Society of Nuclear Medicine and Molecular Imaging, and the Alzheimer's Association. J Nucl Med 2013;54:476–90.

[11] Hou CE, Carlin D, Miller BL. Non-Alzheimer's disease dementias: anatomic, clinical, and molecular correlates. Can J Psychiatry 2004;49:164–71.

[12] Clark CM, Pontecorvo MJ, Beach TG, Bedell BJ, Coleman RE, Doraiswamy PM, et al. A.-A.S. Group. Cerebral PET with florbetapir compared with neuropathology at autopsy for detection of neuritic amyloid-beta plaques: a prospective cohort study. Lancet Neurol 2012;11:669–78.

[13] Sabri O, Sabbagh MN, Seibyl J, Barthel H, Akatsu H, Ouchi Y, et al. G. Florbetaben Phase 3 Study. Florbetaben PET imaging to detect amyloid beta plaques in Alzheimer's disease: phase 3 study. Alzheimers Dement 2015;11:964–74.

[14] Curtis C, Gamez JE, Singh U, Sadowsky CH, Villena T, Sabbagh MN, et al. Phase 3 trial of flutemetamol labeled with radioactive fluorine 18 imaging and neuritic plaque density. JAMA Neurol 2015;72:287–94.

[15] Wang L, Benzinger TL, Su Y, Christensen J, Friedrichsen K, Aldea P, et al. Evaluation of tau imaging in staging Alzheimer disease and revealing interactions between beta-amyloid and tauopathy. JAMA Neurol 2016;73:1070–7.

[16] Noble JM, Scarmeas N. Application of pet imaging to diagnosis of Alzheimer's disease and mild cognitive impairment. Int Rev Neurobiol 2009;84:133–49.

[17] Grimmer T, Wutz C, Alexopoulos P, Drzezga A, Forster S, Forstl H, et al. Visual versus fully automated analyses of 18F-FDG and amyloid PET for prediction of dementia due to Alzheimer disease in mild cognitive impairment. J Nucl Med 2016;57:204–7.

[18] Dubois B, Hampel H, Feldman HH, Scheltens P, Aisen P, Andrieu S, et al. G. Proceedings of the Meeting of the International Working, A.D. the American Alzheimer's Association on "The Preclinical State of, July, U.S.A. Washington Dc. Preclinical Alzheimer's disease: Definition, natural history, and diagnostic criteria. Alzheimers Dement 2016;12:292–323.

[19] Davies P, Maloney AJ. Selective loss of central cholinergic neurons in Alzheimer's disease. Lancet 1976;2:1403.

[20] Bartus RT, Dean RL 3rd, Beer B, Lippa AS. The cholinergic hypothesis of geriatric memory dysfunction. Science 1982;217:408–14.

[21] Coyle JT, Price DL, DeLong MR. Alzheimer's disease: A disorder of cortical cholinergic innervation. Science 1983;219:1184–90.

[22] Perry EK, Perry RH, Blessed G, Tomlinson BE. Changes in brain cholinesterases in senile dementia of Alzheimer type. Neuropathol Appl Neurobiol 1978;4:273–7.

[23] Mesulam MM, Geula C. Butyrylcholinesterase reactivity differentiates the amyloid plaques of aging from those of dementia. Ann Neurol 1994;36:722–7.

[24] Darvesh S. Butyrylcholinesterase as a diagnostic and therapeutic target for Alzheimer's disease. Curr Alzheimer Res 2016;13:1173–7.

[25] Ota T, Shinotoh H, Fukushi K, Nagatsuka S, Namba H, Iyo M, et al. A simple method for the detection of abnormal brain regions in Alzheimer's disease patients using [11C]MP4A: comparison with [123I] IMP SPECT. Ann Nucl Med 2004;18:187–93.

[26] Kuhl DE, Koeppe RA, Snyder SE, Minoshima S, Frey KA, Kilbourn MR. In vivo butyrylcholinesterase activity is not increased in Alzheimer's disease synapses. Ann Neurol 2006;59:13–20.

[27] Irie T, Fukushi K, Namba H, Iyo M, Tamagami H, Nagatsuka S, et al. Brain acetylcholinesterase activity: Validation of a PET tracer in a rat model of Alzheimer's disease. J Nucl Med 1996;37:649–55.

[28] Pappata S, Tavitian B, Traykov L, Jobert A, Dalger A, Mangin JF, et al. In vivo imaging of human cerebral acetylcholinesterase. J Neurochem 1996;67:876–9.

[29] Snyder SE, Tluczek L, Jewett DM, Nguyen TB, Kuhl DE, Kilbourn MR. Synthesis of 1-[11C]methylpiperidin-4-yl propionate ([11C]PMP) for in vivo measurements of acetylcholinesterase activity. Nucl Med Biol 1998;25:751–4.
[30] Namba H, Fukushi K, Nagatsuka S, Iyo M, Shinotoh H, Tanada S, et al. Positron emission tomography: quantitative measurement of brain acetylcholinesterase activity using radiolabeled substrates. Methods 2002;27:242–50.
[31] Kikuchi T, Zhang MR, Ikota N, Fukushi K, Okamura T, Suzuki K, et al. N-[18F]fluoroethylpiperidin-4-ylmethyl butyrate: a novel radiotracer for quantifying brain butyrylcholinesterase activity by positron emission tomography. Bioorg Med Chem Lett 2004;14:1927–30.
[32] Snyder SE, Gunupudi N, Sherman PS, Butch ER, Skaddan MB, Kilbourn MR, et al. Radiolabeled cholinesterase substrates: in vitro methods for determining structure-activity relationships and identification of a positron emission tomography radiopharmaceutical for in vivo measurement of butyrylcholinesterase activity. J Cereb Blood Flow Metab 2001;21:132–43.
[33] Ota T, Shinotoh H, Fukushi K, Kikuchi T, Sato K, Tanaka N, et al. Estimation of plasma IC50 of donepezil for cerebral acetylcholinesterase inhibition in patients with Alzheimer disease using positron emission tomography. Clin Neuropharmacol 2010;33:74–8.
[34] Roivainen A, Rinne J, Virta J, Jarvenpaa T, Salomaki S, Yu M, et al. Biodistribution and blood metabolism of 1-11C-methyl-4-piperidinyl n-butyrate in humans: an imaging agent for in vivo assessment of butyrylcholinesterase activity with PET. J Nucl Med 2004;45:2032–9.
[35] Geula C, Mesulam MM. Cholinesterases and the pathology of Alzheimer disease. Alzheimer Dis Assoc Disord 1995;9:23–8.
[36] Geula C, Greenberg BD, Mesulam M-M. Cholinesterase activity in the plaques, tangles and angiopathy of Alzheimer's disease does not emanate from amyloid. Brain Res 1994;644:327–30.
[37] Guillozet AL, Smiley JF, Mash DC, Mesulam MM. Butyrylcholinesterase in the life cycle of amyloid plaques. Ann Neurol 1997; 42:909–18.
[38] Darvesh S, Reid GA, Martin E. Biochemical and histochemical comparison of cholinesterases in normal and Alzheimer brain tissues. Curr Alzheimer Res 2010;7:386–400.
[39] Macdonald IR, Reid GA, Pottie IR, Martin E, Darvesh S. Synthesis and preliminary evaluation of phenyl 4-123I-iodophenylcarbamate for visualization of cholinesterases associated with Alzheimer disease pathology. J Nucl Med 2016;57:297–302.
[40] Macdonald IR, Reid GA, Joy EE, Pottie IR, Matte G, Burrell S, et al. Synthesis and preliminary evaluation of piperidinyl and pyrrolidinyl iodobenzoates as imaging agents for butyrylcholinesterase. Mol Imaging Biol 2011;13:1250–61.
[41] Oakley H, Cole SL, Logan S, Maus E, Shao P, Craft J, et al. Intraneuronal beta-amyloid aggregates, neurodegeneration, and neuron loss in transgenic mice with five familial Alzheimer's disease mutations: potential factors in amyloid plaque formation. J Neurosci 2006; 26:10129–40.
[42] Darvesh S, Reid GA. Reduced fibrillar beta-amyloid in subcortical structures in a butyrylcholinesterase-knockout Alzheimer disease mouse model. Chem Biol Interact 2016;259:307–12.
[43] Reid GA, Darvesh S. Butyrylcholinesterase-knockout reduces brain deposition of fibrillar beta-amyloid in an Alzheimer mouse model. Neuroscience 2015;298:424–35.
[44] Mikalsen A, Andersen RA, Alexander J. Use of ethopropazine and BW 284C51 as selective inhibitors for cholinesterases from various species. Comp Biochem Physiol C 1986;83:447–9.
[45] Macdonald IR, DeBay DR, Reid GA, O'Leary TP, Jollymore CT, Mawko G, et al. Early detection of cerebral glucose uptake changes in the 5XFAD mouse. Curr Alzheimer Res 2014;11:450–60.
[46] Loening AM, Gambhir SS. AMIDE: A free software tool for multimodality medical image analysis. Mol Imaging 2003;2:131–7.
[47] Ma Y, Hof PR, Grant SC, Blackband SJ, Bennett R, Slatest L, et al. A three-dimensional digital atlas database of the adult C57BL/6J mouse brain by magnetic resonance microscopy. Neuroscience 2005; 135:1203–15.
[48] Woods RP, Grafton ST, Holmes CJ, Cherry SR, Mazziotta JC. Automated image registration: I. General methods and intrasubject, intramodality validation. J Comput Assist Tomogr 1998;22:139–52.
[49] Perry E, McKeith I, Ballard C. Butyrylcholinesterase and progression of cognitive deficits in dementia with Lewy bodies. Neurology 2003; 60:1852–3.
[50] Xiao Y, Guan ZZ, Wu CX, Li Y, Kuang SX, Pei JJ. Correlations between cholinesterase activity and cognitive scores in post-ischemic rats and patients with vascular dementia. Cell Mol Neurobiol 2012; 32:399–407.